International Journal of Engineering

Journal Homepage: www.ije.ir

Mapping Hydrothermal Alteration Zones Associated with Copper Mineralization using ASTER Data: A Case Study from the Mirjaveh Area, Southeast Iran

M. Hosseini Nasab*, A. Agah

Mining Department, University of Sistan and Baluchestan, Zahedan, Iran

PAPER INFO

Paper history:
Received 29 May 2022
Received in revised form 22 January 2023
Accepted 03 February 2023

Keywords:
Mirjaveh
Hydrothermal Alteration
Copper Exploration
Principal Components Analysis
Logical Operator
Spectral Angle Mapper

ABSTRACT

In this research, ASTER satellite images and the combined algorithm of band ratios with the method of logical operators with the determination of the threshold limit based on ground, laboratory and experimental studies have been used in order to highlight hydrothermal alterations. Image transformation techniques such as specialized band ratio and principal component analysis are used to map lithologic units and alteration minerals. Supervised classification technique, i.e. Spectral Angle Mapper (SAM) is applied to detect subtle differences between index alteration minerals associated with actual copper localities in the region. The results show that the integration of image transformation techniques and supervised classification of ASTER data with field studies and geochemical exploration is highly effective in targeting new copper mineralization prospects. Copper mineralization is found in siliceous veins that strike from north-south to northeast-southwest across the region. Remote sensing evidence supports the presence of propylitic and argillic alteration, which can be useful for searching for copper-gold type deposits. Kaolinite and pyrophyllite play a role in identifying arzilic alteration zones, and muscoite, epidote and chlorite minerals are very important in identifying pyropilitic and phyllic areas and in mineral exploration. Based on remote sensing processing, according to the detection of various alterations (phyllic, pyrophyllite and argillic) in this area, possible copper mineralization was detected in the central part of the studied area. The approach used in this research provides a quick and cost-effective means of initiating comprehensive geological and geochemical exploration programs in the study area and elsewhere in similar areas.

***doi**: 10.5829/ije.2023.36.04a.11*

1. INTRODUCTION

Today, remote sensing is critical in geological projects because it can offer important information on structural examinations such as alteration zone identification, line extraction, geomorphological phenomena, and so on. The use of remote sensing to detect alteration zones for the purpose of mineral exploration goes back to the 1970s [1]. The study of wallrock alteration may give significant information on the mineralization type, characteristics of mineralizing solutions, physicochemical conditions of minerals, and mineralization depth since the same rock-type ores cause the wallrock alteration. Another benefit of researching alteration mineral zones is that they are frequently utilized as a useful guide for mineral exploration owing to their greater extension compared to mineral horizons and simpler recognition of such zones in the desert because of color and other physical characteristics.

The most common uses of satellite remote sensing data for regional-scale mineral survey projects in the past decade have been mineral discovery via hydrothermal alteration and mapping of structural geology [1-16]. The phyllic alteration region is typically defined by pyrite-quartz-sericite rocks with a high OH-Al absorbance peak at 2.20 μm, which corresponds to Advanced Spaceborne Thermal Emission and Reflection Radiometer band 6 [3]. Supergene processes often influence the argillic alteration region. Plagioclase is chemically changed to different clay minerals (such as montmorillonite, kaolinite, and illite), which collectively exhibit an OH-Al absorbance peak at 2.17 μm, which corresponds to

*Corresponding Author Email: hosseininasab@eng.usb.ac.ir
(M. Hosseini Nasab)

Please cite this article as: M. Hosseini Nasab, A. Agah, Mapping Hydrothermal Alteration Zones Associated with Copper Mineralization using ASTER Data: A Case Study from the Mirjaveh Area, Southeast Iran, ***International Journal of Engineering, Transactions A: Basics***, Vol. 36, No. 04, (2023), 720-732

Advanced Spaceborne Thermal Emission and Reflection Radiometer band 5. The mineralogy of magnetite, pyrite, sericite, chlorite, carbonates and epidote in the propylitic alteration region is varied, with Fe-OH, Mg absorbance peaks in the 2.35 μm, which corresponds to Advanced Spaceborne Thermal Emission and Reflection Radiometer band 8 [17].

Multispectral remote sensing sensors including the Advanced Spaceborne Thermal Emission and Reflection Radiometer (ASTER), Landsat Multispectral Scanner (MSS), Landsat Thematic Mapper/Enhanced Thematic Mapper+ (TM/ETM+), HyMap, the Airborne Visible/Infrared Image Spectrometer (AVIRIS), and Hyperion hyperspectral have been successfully and extensively used for mapping alteration mineral assemblies and fractures/faults related to exploring copper deposits, which is a critical component in the discovery of copper resources [1, 18-23].

Since the 1970s, remote sensing data has been an indispensable tool for determining changes. The Landsat series of satellite sensors, including TM, ASTER, and ETM, provide vast and ongoing data for the investigation of a range of ores. The governing concept is that different minerals have different VNIR and SWIR spectrum properties. Crosta and Moore were the first to utilize TM data to derive modification information in the 1980s. Researchers utilized TM pictures to extract mineral alteration information using the band ratio technique and Principal Components Analysis (PCA) toward the end of the twentieth century [24]. Many researchers expanded innovative methods to extract alteration and mineralization information in the early twenty-first century, which resulted in effective prospecting findings [9, 25-35]. Crosta et al. [36] were the first to utilize PCA and ASTER data to extract alteration data in Patagonia, Argentina. Other researchers later used ASTER data to achieve important achievements in a variety of fields [37-45].

A comprehensive remote sensing research for copper exploration in the Mirjaveh area, which is situated in the Nehbandan-Khash zone (in Iran's southeast), has not yet been reported. Based on this, the goals of this research are: (1) to indicate the hydrothermal alteration map of minerals and geological structural features such as faults and fractures related to copper mineralization in Mirjaveh region using ASTER satellite data. (2) to prospect of areas with high potential of copper mineralization using the integration of robust image processing techniques into ASTER spectral and thermal bands. and (3) to develop a cost-effective exploration approach to explore for copper mineralization in the region and other remote areas around the world.

2. GEOLOGIC SETTINGS

The investigated region is found on the geological maps of Zahedan (1: 250,000) and Mirjaveh (1: 100000), as well as in Iran's Nehbandan-Khash zone (Figure 1).

The western boundary of the Nehbandan-Khash zone is the Nehbandan fault, while the southern edge with the Makran is the Bashagard fault region. The eastern edge of the Nehbandan-Khash zone is west of Afghanistan and Pakistan, and the western border is the Nehbandan fault. This zone is also known as the colored melange zone because of the presence of melange ophiolites in eastern Iran [46]. The Nehbandan-Khash flysch basin, according to recent research [47, 48], is the weld zone between the Afghanistan and Lut block, or the Sistan weld region. The zone is divided by a sedimentary environment (Sefidabeh basin) into two assemblages of ophiolitic melange (Retuk assemblages in the west, but not in the east). The region includes basal volcanic, metamorphic (schistose structure) strata, and intrusive masses, the newest of which is Quaternary alluvial deposits, according to stratigraphic investigations on the map of Mirjavah (scale 1:500,000) (Figure 2). Due to the temporal range of rock sequences, this region is geologically young, and its Quaternary deposits are made up of a variety of rock sequences. In the research region, the most well-known rock sequences are:

A) The fault system limits, severely breaks, and deforms tectonic mixes (colored melanges) composed of basaltic to ultrabasic rocks with blocks of serpentine ultrabasic, which frequently protrude in the form of a narrow strip in the region.
B) Intrusive mass
C) Metamorphic rocks
D) Alluvial sediments
F) Terrigenous sedimentary rocks

2. 1. Geology of Deposit Area The zone is located in the Nehbandan-Khash region, and it contains a tiny portion of the Mirjaveh (scale 1: 100000). Sandstone, siltstone, mudstone, and volcanic sandstone, as well as lime, tuff, and alluvial deposits, make up the majority of the exploration area.

Copper mineralization may be seen in the region in the shape of siliceous veins. The main trend of copper mineralized siliceous veins is north-south to northeast-southwest. Most shale strata and tectonized sandstone, as well as volcanic rocks (p^{sv}), have been cut by these siliceous veins. Mineralization effects are visible in the shape of space-filling in the rock fractures and joints, and the rock orientation is shear. In addition, iron oxides and hydroxides act as cement in the formation of rock.

Mineralizing streaks are often controlled by northeast-southwest faults. With modest halos of argillic and sericite changes, the argillic and siliceous alterations are the most common. Iron hydroxides and potentially copper ores, have formed in the oxidant fraction as a result of secondary reactions.

Faults of various lengths and orientations may be found in this region. Faults having a northeast-southwest

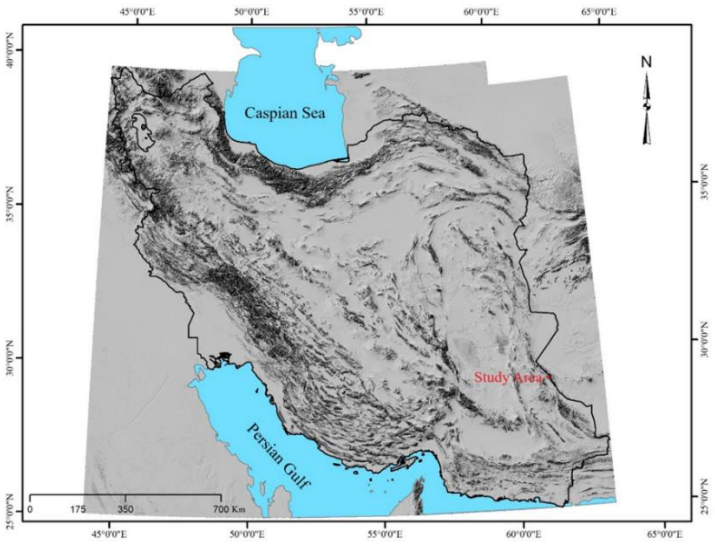

Figure 1. Image of Iran from a digital elevation model (DEM), showing the research area's location

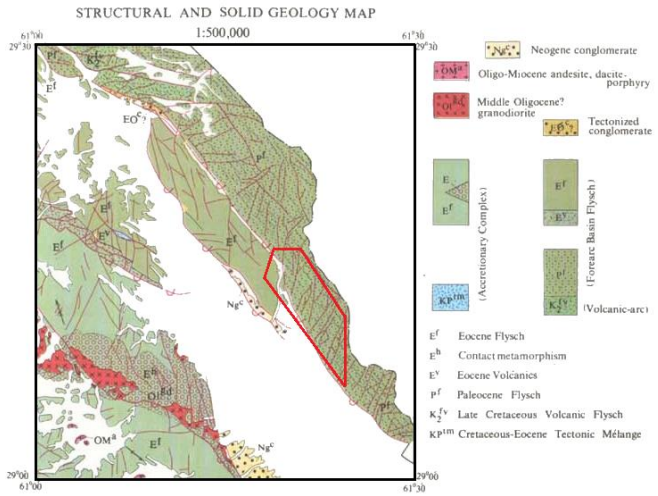

Figure 2. The studied area on a geological 1: 500000 map of Mirjaveh

extension, on the other hand, are more common and primarily regulate mineralization processes.

According to the Mirjaveh map (scale 1: 500000), the research area's outcrop units, from old to new, are as follows:

- Paleocene units:

(P^{sv2}): Tuff, lapilli tuff, mudstone, and sandstone are all found in this unit. The unit's main trend is northwest-southeast, and it has a wide dispersion throughout the area.

(P^{sv4}): This Paleocene unit contains a wide range of rock types, including mudstone, siltstone, green shale, and lime. This unit's main trend is northwest-southeast.

- Eocene units:

(E^{s2}): This Eocene unit contains siltstone, mudstone, and grain-size sandstones with a little olive to grey, purple, or blue thin-layer lime. The dynamo-thermal technique was used to change this unit. As a result, all of the stones have been somewhat changed. In fine-grained sediments, phyllic and slate tissues associated with sericite growth are common. Sandstones are typically granular, and they may crystallize into schist or coarse quartzite. This unit's main trend is northwest-southeast.

- The Oligocene unit:

(EO^{c}): This Oligocene unit, which comprises conglomerate and sandstone, has a limited distribution throughout the region. This unit's main trend is northwest-southeast.

- Quaternary units:

(Q^{f1}): This category includes older alluvial fans with vegetation and numerous terraces (t^{1}).

Alluvial sediments of the present era (Q^{al}):

The Qal mark on the map distinguishes the alluvial sediment samples of the current period that develop around seasonal rivers from other alluvial deposits. These newly formed and deposited sediments are still being produced and deposited.

3. METHODOLOGY

ASTER satellite images are processed for remote sensing interpretation. The following methods demonstrated the ability of ASTER images to provide data for the detection of hydrothermal alteration useful for mineral exploration. In addition, the techniques used in the study area are useful for identifying mineralization zones with high potential. Using logic operator mapping algorithms, PCA and SAM methods, Landsat ASTER image data of the study area were processed to map hydrothermal alteration zones.

3. 1. Remote Sensing Data Characteristics and Pre-processing In 1999, the ASTER sensor was launched as part of the TERRA satellite. This sensor offers 14 distinct bands of spectral data for ground resources. There are three bands in the near-infrared and visible spectra (52%-86%), with a spatial resolution of 15 m and three-dimensional vision provided by the BACKWARD and NADIR components. In addition, there are six bands in the shortwave infrared spectra (1.6-2.43) with a spatial resolution of 30 m. Moreover, there are five bands in the thermal infrared spectra (5.125-11.650), with a spatial resolution of 90 m (Table 1).

The data from ASTER level 1T has been geometrically and radiometrically adjusted. The pixel amounts of the ASTER L1T are the sensor's radiance value. The atmospheric correction module was used to extract surface leaving radiance data and remove the effects of air scattering and absorption. In the present study, the SWIR and VNIR bands of the ASTER were additionally corrected using the Fast Line-of-Sight Atmospheric Analysis of Spectral Hypercubes (FLAASH) algorithm. The ASTER 30-m resolution SWIR bands were resampled to match the 15-m resolution VNIR bands in order to apply the image processing techniques. To retain the original pixel amounts in the resampled pictures, the nearest neighbor resampling technique was used.

3. 2. Image Processing Methods In the present study, various image processing techniques, such as band ratio, false-color combination, and principal component analysis, were utilized to detect changed areas. The features of each method, as well as the outcomes, are given in the following sections.

3. 2. 1. False Color Combination Method The false-color combination was utilized to visually understand the changed regions using satellite data. Due to adsorption, the minerals kaolinite, halloysite, muscovite, dickite, and pyrophyllite (index of phyllic and argillic alteration zones) exhibit a high reflection in SWIR band 4 and a low reflection in band 6 according to standard curves (Figure 3). Furthermore, the minerals chlorite, calcite, and epidote (propylitic zone index) are

TABLE 1. ASTER sensor specifications

Spectrometer	Band	Wavelength (μm)	Radiometric resolution (bits)	Spatial resolution (m)
VNIR	1	0.520-0.600	8	15
	2	0.630-0.690	8	15
	N3	0.780-0.860	8	15
	B3	0.780-0.860	8	15
SWIR	4	1.600-1.700	8	30
	5	2.145-2.185	8	30
	6	2.185-2.225	8	30
	7	2.235-2.285	8	30
	8	2.295-2.365	8	30
	9	2.360-2.430	8	30
TIR	10	8.125-8.475	12	90
	11	8.475-8.825	12	90
	12	8.925-9.275	12	90
	13	10.25-10.95	12	90
	14	10.95-11.65	12	90

reflected the least in band 8 and the most in bands 5 and 4 (Figure 4).

Bands 8, 6, and 4 of ASTER are shown in Figure 5 as a red-green–blue composite. The separation of the various spectral changes and lithological units in the research region is visualized and enhanced using this false-color composite. The chosen bands are the most effective for creating a color composite because they correspond to the absorption characteristics of the argillic, propylitic, and phyllic zones. Figure 5 depicts the majority of lithological units with spectral characteristics linked to Mg-Fe-OH and Al-OH minerals. Because of the high reflection in band 4 and strong absorbance characteristics in band 6, argillic and phyllic alteration zones with significant Al-OH absorbance features (halloysite, muscovite, kaolinite, dickite, and pyrophyllite minerals) show as a pinkish shade. In band 8, propylitic alteration zones (chlorite, epidote, and calcite minerals) are shown in green tone owing to Fe-OH-Mg absorbance characteristics (chlorite, epidote, calcite minerals). Bold pink pixels may be seen in certain regions of this type, which are associated with places with extensive argillic alteration (alunite).

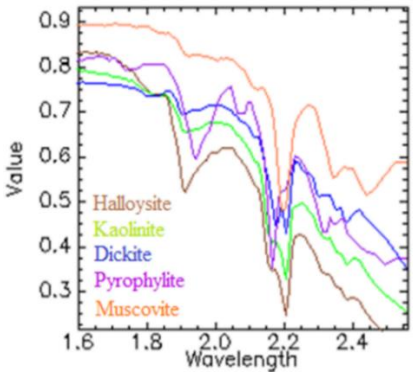

Figure 3. Reflection of argillic and phyllic index minerals in the USGS standard curve

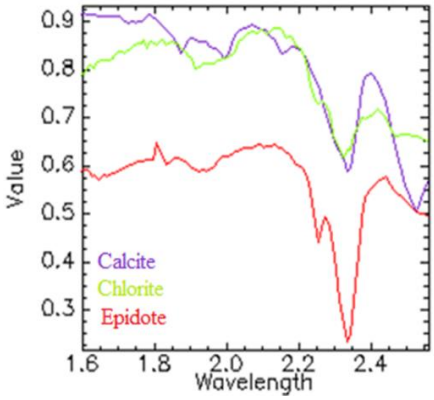

Figure 4. Reflection of propylitic index minerals in the USGS standard curve

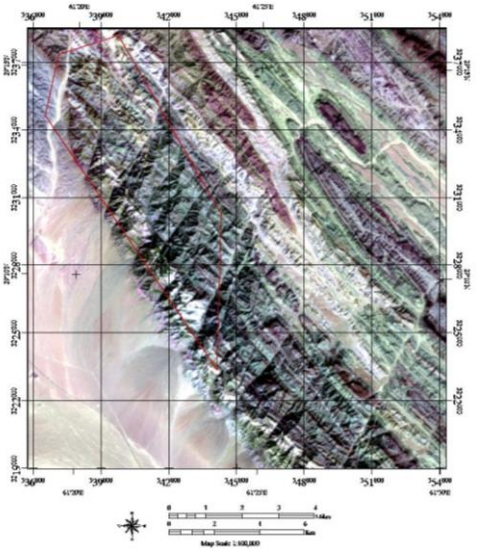

Figure 5. The false-color combination of 468 ASTAR sensors (argillic alteration in pink and propylitic alteration in green) is visible

3. 2. 2. Logical Operator Mapping Algorithms

For each pixel, the logic operator's algorithm is specified based on a combination of different band ratios. In this study, for the study range of a series of band ratios to define the algorithm associated with silica-rich hydrothermal zones (hydro silica, chalcedony and opal), Propylitic alteration in relation to carbonate and chlorite-epidote minerals separately, argillic alteration in the presence of alunite-kaolinite minerals and phyllite alteration with sericite-muscovite index minerals have been used algorithms according to Table 2. Finally, the logic operators used for these purposes each provide a definite value of true (value one for the desired pixel) or false (value of zero for the desired pixel) for each pixel of the image. For each algorithm for the target, an image is generated with pixel value values of one and zero, which specifies pixels with a value equal to a target area. Each of these band ratios in the defined algorithm has a specific threshold value. This value is calculated based on statistical methods from relative images using Equation (1) and is used as a suitable coefficient in combining different band ratios in Table 2. It is worth noting that in certain cases this value has been changed due to experience and knowledge of the study area.

$$\text{Threshold}=\mu+2\sigma \quad (1)$$

In this regard, μ is the mean and σ are the standard deviations.

For all operators defined in the algorithms, a band ratio of 3 to 2 is used to mask the vegetation. In order to map areas with high silica, the band ratio of 4 to 7 in the SWIR range shows areas with high alteration. For silica minerals, regions with the presence of alteration have less

TABLE 2. Logical operator algorithms used to map altered rocks in area study

Alteration type	Algorithm
Phyllic	(float(b3)/(b2) le 1.22) and (float(b4)/(b6) gt 1.22) and (float(b5)/(b6) gt 1.15) and (float(b7)/ (b6) ge 1.02)
Argillic	(float(b3)/(b2) le 1.22) and (float(b4)/(b6) gt 1.22) and (float(b5)/(b6) le 1.15) and (float(b7)/(b6) ge 1.02)
Propylitic (Calcite-Dolomite)	(float(b3)/(b2) le 1.22) and (float(b6)(/b8) gt 0.83) and (float(b13)/(b14) gt 0.94) and (b5 gt b6) and (b7 gt b8) and (b9 gt b8)
Propylitic (Epidote-chlorite)	(float(b3)/(b2) le 1.22) and (float(b6)/(b8) gt 0.83) and (float(b13)/(b14) le 0.94) and (float(b5)/float(b4+b6)) and (b5 gt b6) and (b6 gt b7)and (b7 gt b8) and (b9 gt b8)
Silica-rich hydrothermal alteration	(float(b3)/(b2) le 1.22) and (float(b4)/(b7) gt 1.24) and float(b13)/(b12) gt 1.34) and (float(b12)/ (b11) ge 1.13)

reflection at wavelengths between 2 and 2.4 μm than regions without alteration. The reason for this is the property of adsorption of water molecules in the range of 2.26 to 2.4 micrometers. The bandwidth ratio of the TIR range of ester images to highlight high silica areas using a 13 to 12 bandwidth ratio with absorption at a wavelength of 9.619 μm, so high silica areas are characterized by non-alteration areas by reflecting each pixel in the SWIR area. To identify rocks containing silica-rich hydrothermal alterations, an image with a value of one pixel for target points and zero for other points in the algorithm was prepared. Figure 6 shows the silica-rich hydrothermal zones.

Mapping of propylitic hydrothermal alteration has been characterized using band ratios defined in the SWIR and TIR spectral ranges. The spectral adsorption index of calcite at 11.2 μm and chlorite-epidote with adsorption at 10.2 μm were used to isolate propylitic alteration associated with carbonate and epidote-chlorite minerals (Figure 7). Emission of calcite in the upper 13 band and is less in band 14, while it is the opposite for epidote and chlorite (Figure 8). In the logical operator defined for the separation of propylitic alteration with two classes of calcite and epidote-chlorite minerals from the band ratio of 6 to 8 in the SWIR range to highlight the adsorption of both groups at a wavelength of 2.31 to 2.33 μm and to separate the two froms. The band ratio of 13 to 14 in the TIR range of the ester image has been revealed by selecting the threshold of 0.94, two groups of indicators of this alteration.

Detection of argillic and phyllite alterations in the SWIR range of ester images has been used to map the OH-Al adsorption spectrum with a band ratio of 4 to 5 at 2.165 μm and a band ratio of 4 to 6 at 2.2 μm, respectively. A band ratio of 5 to 6 has been used to distinguish between the two alterations. The 7 to 6 band ratio is used to display pixels with a wavelength of 2.2 μm for argillic and phyllite alteration. Figures 9 and 10 show the manifestations of these alterations in the study area.

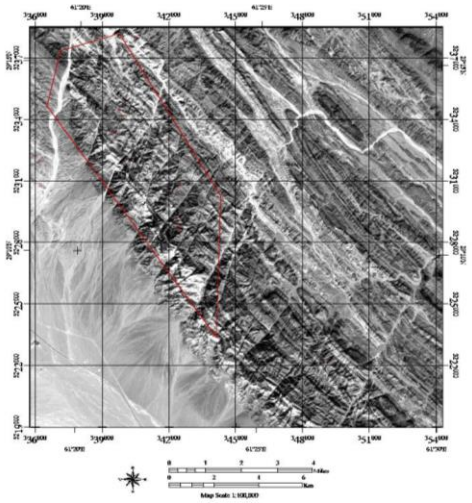

Figure 6. Maps of Silica-rich hydrothermal alteration using logical operator algorithms include

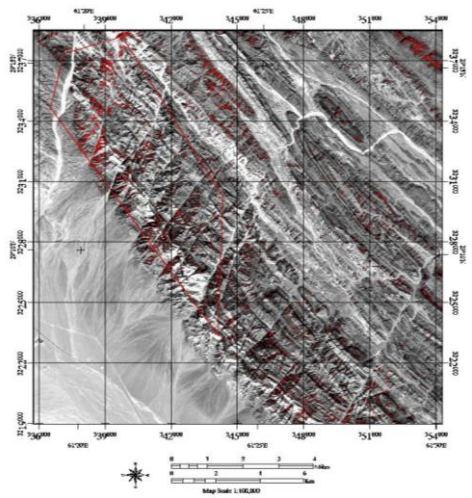

Figure 7. Maps of propylitic rocks (epidote-cholerite) using logical operator algorithms include

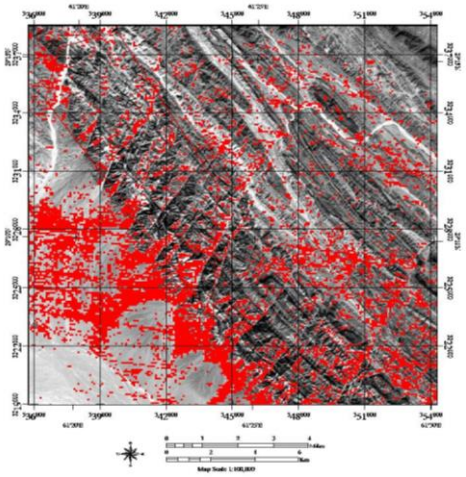

Figure 8. Maps of propylitic rocks (calecite-dolomite) using logical operator algorithms include

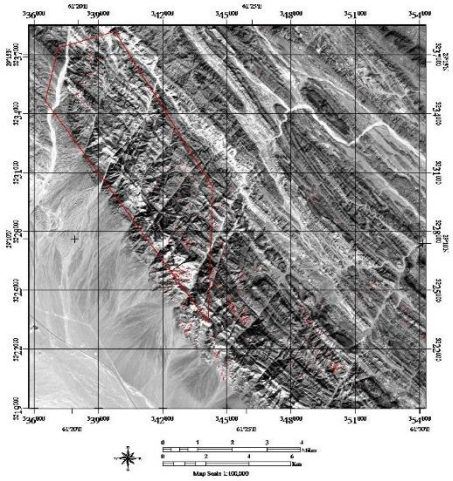

Figure 9. Maps phyllic rocks using logical operator algorithms include

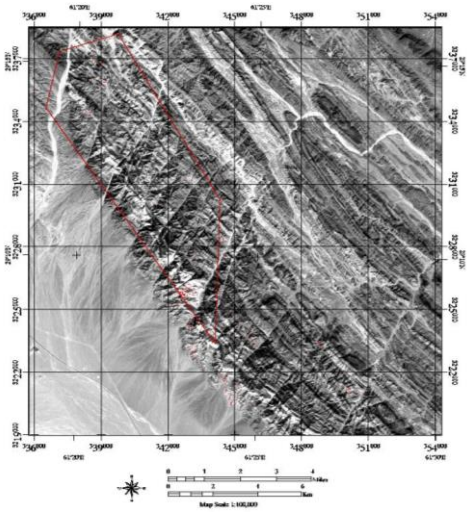

Figure 10. Maps of argillic rocks using logical operator algorithms include

3. 2. 3. Principal Component Analysis Method

By selecting multiple sets of principle components and decreasing dimensions, principal component analysis in ENVI5.3 is a commonly used technique for isolating noise and extracting mineral information. Different minerals that have experienced the same modification have undergone comparable geologic occurrences and have chemical compositions that are similar. In this research, PCA was used to map the particular changes of interest utilizing the ASTER VNIR+SWIR bands. For identifying zones of hydrothermal alteration associated with Cu mineralization, the absorbance characteristics of indicator minerals were examined. A PC picture may improve a mineral or mineral group by including eigenvector loadings that contain unique contributions (sign and magnitude) for absorbance and reflective bands of alteration minerals or mineral groups. The picture tone for the improved target mineral will be bright if the loading in the reflective band of the mineral is positive and dark if it is negative [49].

In this research, principal component analysis was initially conducted on ASTER bands 1-9. Based on the phyllic modification index minerals' reflection in band 7 and their absorbance in band 6 in principal component analysis, PC5 reveals the most important difference in the eigenvector of these two bands. Thus, this PC was identified to be the most suited PC for the recognition of phyllic alteration and epithermal Cu mineralization. Figure 11 depicts the final picture. In principal component analysis, PC4 was selected as the most appropriate PC to show this alteration based on the reflection of index minerals of argillic alteration (kaolinite) in band 5 and their absorbance in band 6. Figure 12 depicts the picture produced from this study. PC9 was selected as the most appropriate to exhibit this alteration picture produced from this study based on the

reflection of index minerals of propylitic alteration (epidote, chlorite) in band 9 and their absorbance in band 8. The white pixels in this picture indicate propylitic modification (Figure 13). Figure 14 depicts a color picture of PCs obtained for various modifications.

Based on the eigenvector matrix of the ASTER bands obtained from the PCA, the PC4, PC9, and PC5 pictures may include spectral information linked to argillic, propylitic, and phyllic alteration zones (Table 3). From the SWIR and VNIR spectral regions of ASTER, the eigenvector loadings provide suggestive information about the spectral properties of alteration minerals. As a result, a PC with strong eigenvector loadings for suggestive bands of an alteration mineral or mineral group with opposing signs accentuates that mineral or mineral group as bright or dark pixels in the PC picture. Positive loading in a reflecting band accentuates the alteration mineral by depicting it as bright pixels, while negative loading in a reflective band shows it as dark pixels [49].

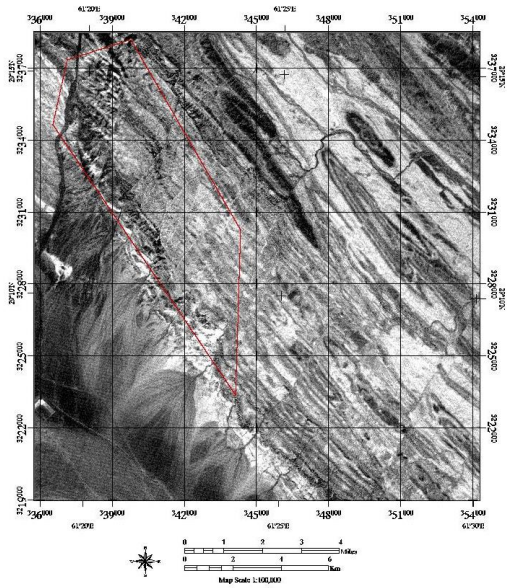

Figure 11. PC5 image of the main components (bright pixels shows phyllic alteration)

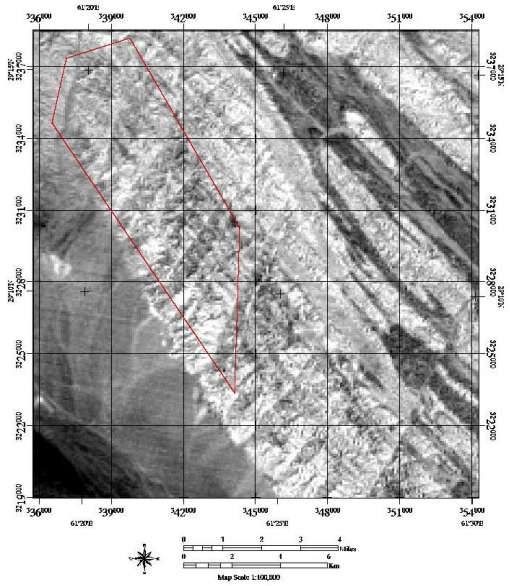

Figure 12. PC4 image of the main components (bright pixels shows argillic alteration)

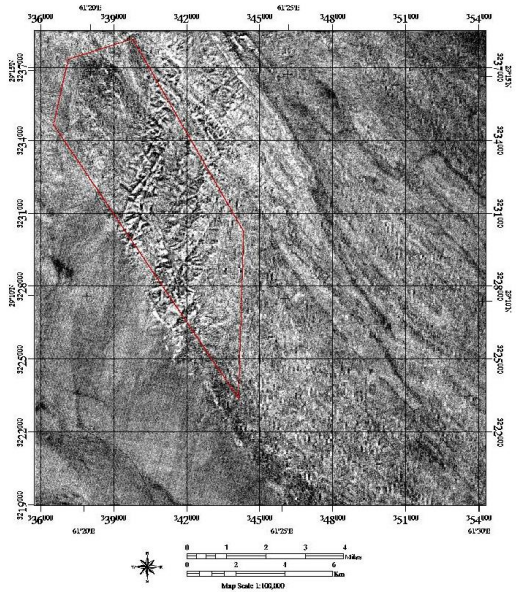

Figure 13. PC9 image of the main components (bright pixels shows propylitic alteration)

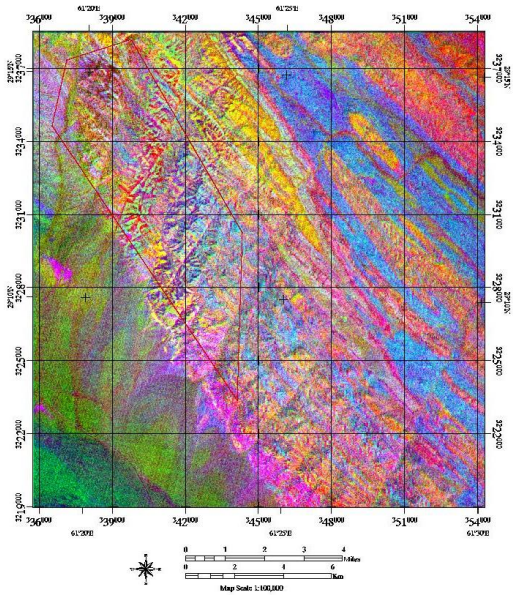

Figure 14. Image of RGB (PC4, PC9, PC5). The red and pink pixels show argillic alteration; the blue part specifies the phyllic alteration. The green pixels show propylitic alteration

TABLE 3. Eigenvector matrix of Principal Components Analysis (PCA) on *VNIR and* SWIR bands of ASTER data

Eigenvector	Band 1	Band 2	Band 3	Band 4	Band 5	Band 6	Band 7	Band 8	Band 9
PCA1	-0.256	-0.286	-0.291	-0.325	-0.273	-0.275	-0.273	-0.260	-0.320
PCA2	0.159	0.172	0.178	0.186	0.162	0.153	0.151	0.149	0.217
PCA3	0.472	0.510	0.434	-0.195	-0.293	-0.261	-0.217	-0.170	-0.238
PCA4	-0.050	-0.008	0.050	0.134	**0.101**	**-0.013**	-0.137	-0.094	0.092
PCA5	-0.509	0.029	0.360	0.218	-0.431	**-0.438**	**0.118**	0.366	0.172
PCA6	-0.085	0.052	0.004	0.745	0.138	-0.072	-0.038	-0.187	-0.593
PCA7	0.410	0.019	-0.533	0.222	-0.211	-0.379	0.070	0.162	0.221
PCA8	-0.254	-0.017	0.310	-0.129	0.184	0.087	-0.179	-0.189	0.125
PCA9	-0.039	0.046	-0.043	0.300	-0.012	-0.097	-0.518	**-0.440**	**0.564**

3. 2. 4. Spectral Angle Mapper Algorithm (SAM) The SAM classification method that enables rapid mapping measures the spectral resemblance between the picture spectrums to reflectance spectra reported in the literature [50]. There are three ways to obtain the reference spectra: 1. Taking it from a laboratory, 2. Field measurements, 3. Direct extraction from an image. SAM calculates the spectral semblance by measuring the two spectra's angles, as if they are vectors in n-dimensional space [17]. Small angles forming in-between the two spectra indicate high similitude. Moreover, high angles are indications of dissimilarity. Solar illumination elements do not affect this methodology due to the independency of the angle the two vectors make of their lengths. It takes the arccosine of the dot product between the test spectrums "t" to a reference spectrum "r" with Equation (2) [51]:

$$\alpha=\cos^{-1}\left[\frac{\sum_{i=1}^{nb} t_i r_i}{(\sum_{i=1}^{nb} {t_i}^2)^{1/2}(\sum_{i=1}^{nb} {r_i}^2)^{1/2}}\right] \quad (2)$$

where nb is the number of bands, t_i is test spectrum, r_i is reference spectrum.

The SAM method was proposed by Bordman to measure the spectral similarity between the reference spectrum and the spectrum corresponding to each pixel [19]. In the present study, in the SAM method, the spectrum of each pixel of the ester image is compared with specific dimensions called member-end, which is the maximum absorption in the desired mineral. A variety of minerals from the USGS Spectral Library were used to access the member-end.

The spectral properties of the altered minerals in the SWIR bands of the ester images make it possible to determine the hydrothermal alteration zones using the minerals that are specific to that type of alteration. Muscovite, Illite and Cerussite minerals as the index of phyllite zone and kaolinite mineral as the index of argillic zone and Clacite, Dolomite and Epidote minerals as the index of propylitic zone are the characteristic minerals. The deposits of the area are displayed at a higher magnification around the main map.

In this study, the member-end used for mineral's kaolinite was 6 and 5 bands (2.146-2.225 micrometers) and 6 and 7 bands (2.185-2.285 micrometers). The result of the SAM image is a black and white image whose color intensity is inversely related to the similarity between the member-end number and the spectrum of each particular pixel in the image (Figures 15-18) [52].

3. 3. Field Verification The identified alteration zones from processed ASTER images are verified with in-situ inspection. The field photographs of rock units, copper deposits and the geomorphology in the study area are shown in Figures 19 to 22.

Geological section 1 has a length of 3586 meters and is located in the western corner of the exploration area and has a north-south trend. This profile is composed of volcanic rocks and flysch sediments and is free of mineralization (Figure 19).

The identified alteration zones from processed ASTER images are verified with in-situ inspection. The field photographs of rock units, copper deposits and the geomorphology in the study area are shown in Figures 19 to 22.

Geological section 1 has a length of 3586 meters and is located in the western corner of the exploration area and has a north-south trend. This profile is composed of volcanic rocks and flysch sediments and is free of mineralization (Figure 19).

Geological section 2 has a length of 4546 meters and is located in the center of the exploration area and has a northeast-southwest trend. This profile is composed of volcanic rocks along with flysch units and radiofrequency shales that are intersected by siliceous veins and veins that contain copper mineralization (Figures 20-21).

Geological section 4 has a length of 4060 meters and is located in the west of the exploration area and has a

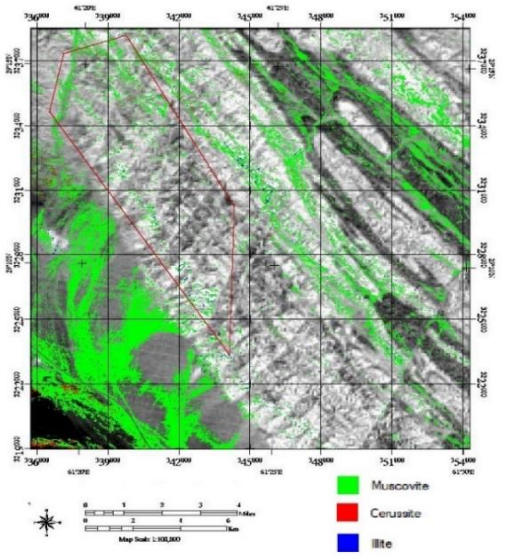

Figure 15. The result of spectral angle mapper (SAM) classification for phyllic zones

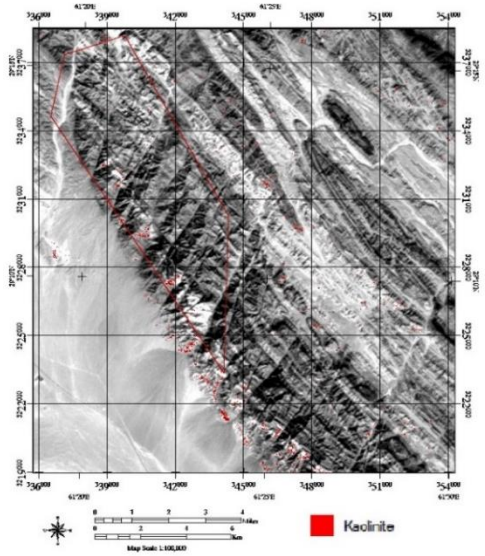

Figure 16. The result of spectral angle mapper (SAM) classification for Argilic zones

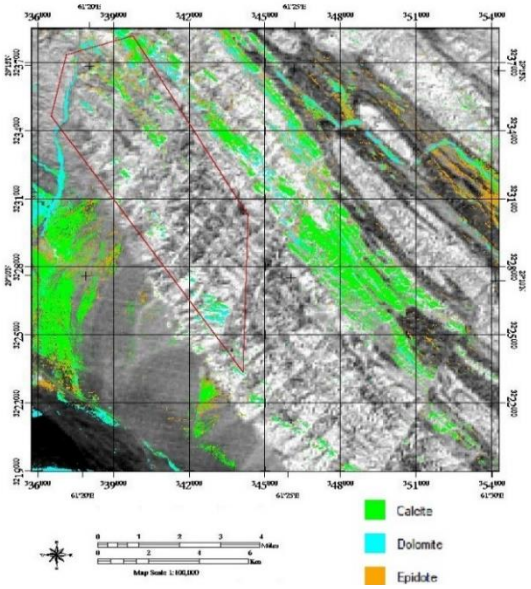

Figure 17. The result of spectral angle mapper (SAM) classification for Propylitic zones

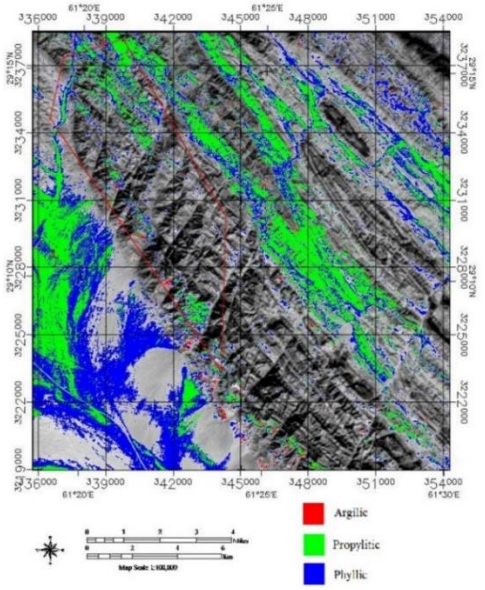

Figure 18. The result of spectral angle mapper (SAM) classification for alteration zones

Figure 19. Units in profile 1

Figure 20. View of copper mineralization in profile 2

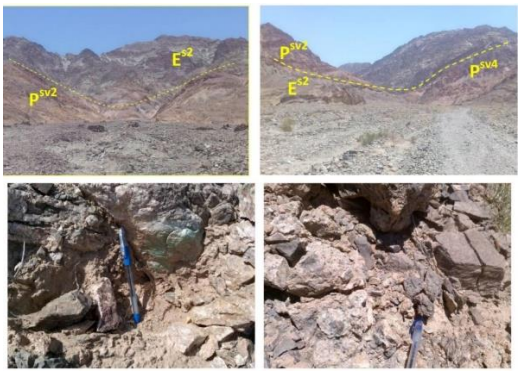

Figure 21. View of copper mineralization in the area along with siliceous veins

Figure 22. Units in profile 3

northeast-southwest trend. This profile is composed of volcanic rocks with flysch units, some of which are cut by siliceous veins and have no mineralization.

Geological section 3 has a length of 4976 meters and is located in the center of the exploration area and has a northwest-southeast trend. This profile is composed of volcanic rocks with flysch units, some of which are cut by siliceous veins and have no mineralization (Figure 22).

4. CONCLUSION

The new information extracted from ASTER specialized logical operators, PCA, and SAM defines several potential zones for copper exploration in Mirjaveh region. Statistical accuracy assessment and fieldwork data also verified the consistency of the results. Finally, based on remote sensing techniques, the diagnosis of potential Cu mineralization in the center portion of the research region was achieved owing to the identification of diverse and widespread changes (phyllic, propylitic, and argillic) in this area. Based on the investigations and their findings, the subsequent phases of exploration in the research area are economically justifiable, and the central, northern, and northwestern portions of the zone are presented as potential locations for exploration stages. This investigation emphasizes how remote sensing data can promote targeting high potential zones for orogenic copper in Mirjaveh in EW Iran and in similar areas elsewhere.

5. REFERENCES

1. Pour, A.B. and Hashim, M., "The application of aster remote sensing data to porphyry copper and epithermal gold deposits", ***Ore Geology Reviews***, Vol. 44, (2012), 1-9. http://dx.doi.org/10.1016/j.oregeorev.2011.09.009
2. Tripp, G.I. and Vearncombe, J.R., "Fault/fracture density and mineralization: A contouring method for targeting in gold exploration", ***Journal of Structural Geology***, Vol. 26, No. 6-7, (2004), 1087-1108. http://dx.doi.org/10.1016/j.jsg.2003.11.002
3. Mars, J.C. and Rowan, L.C., "Regional mapping of phyllic-and argillic-altered rocks in the zagros magmatic arc, iran, using advanced spaceborne thermal emission and reflection radiometer (ASTER) data and logical operator algorithms", ***Geosphere***, Vol. 2, No. 3, (2006), 161-186. https://doi.org/10.1130/GES00044.1
4. Paez, G.N., Ruiz, R., Guido, D.M., Jovic, S.M. and Schalamuk, I., "Structurally controlled fluid flow: High-grade silver ore-shoots at martha epithermal mine, deseado massif, argentina", ***Journal of Structural Geology***, Vol. 33, No. 5, (2011), 985-999. https://doi.org/10.1016/j.jsg.2011.02.007
5. Pour, A.B. and Hashim, M., "Identification of hydrothermal alteration minerals for exploring of porphyry copper deposit using aster data, se iran", ***Journal of Asian Earth Sciences***, Vol. 42, No. 6, (2011), 1309-1323. http://dx.doi.org/10.1016/j.jseaes.2011.07.017
6. Rossetti, F., Aldega, L., Tecce, F., Balsamo, F., Billi, A. and Brilli, M., "Fluid flow within the damage zone of the boccheggiano extensional fault (larderello–travale geothermal field, central italy): Structures, alteration and implications for hydrothermal mineralization in extensional settings", ***Geological Magazine***, Vol. 148, No. 4, (2011), 558-579. http://dx.doi.org/10.1017/S001675681000097X
7. Pour, A.B. and Hashim, M., "Identifying areas of high economic-potential copper mineralization using aster data in the urumieh–dokhtar volcanic belt, iran", ***Advances in Space Research***, Vol. 49, No. 4, (2012), 753-769. http://dx.doi.org/10.1016/j.asr.2011.11.028
8. Alimohammadi, M., Alirezaei, S. and Kontak, D.J., "Application of aster data for exploration of porphyry copper deposits: A case study of daraloo–sarmeshk area, southern part of the kerman copper belt, iran", ***Ore Geology Reviews***, Vol. 70, (2015), 290-304. https://doi.org/10.1016/j.oregeorev.2015.04.010
9. Safari, M., Maghsoudi, A. and Pour, A.B., "Application of landsat-8 and aster satellite remote sensing data for porphyry copper exploration: A case study from shahr-e-babak, kerman, south of iran", ***Geocarto International***, Vol. 33, No. 11, (2018), 1186-1201. https://doi.org/10.1080/10106049.2017.1334834
10. Ahmadirouhani, R., Karimpour, M.-H., Rahimi, B., Malekzadeh-Shafaroudi, A., Pour, A.B. and Pradhan, B., "Integration of spot-5 and aster satellite data for structural tracing and hydrothermal alteration mineral mapping: Implications for cu–au prospecting", ***International Journal of Image and Data Fusion***, Vol. 9, No. 3, (2018), 237-262. https://doi.org/10.1080/19479832.2018.1469548
11. Ge, W., Cheng, Q., Jing, L., Armenakis, C. and Ding, H., "Lithological discrimination using aster and sentinel-2a in the shibanjing ophiolite complex of beishan orogenic in inner mongolia, china", ***Advances in Space Research***, Vol. 62, No. 7, (2018), 1702-1716. https://ui.adsabs.harvard.edu/link_gateway/2018AdSpR..62.1702G/doi:10.1016/j.asr.2018.06.036

12. Yazdi, Z., Jafari Rad, A., Aghazadeh, M. and Afzal, P., "Alteration mapping for porphyry copper exploration using aster and quickbird multispectral images, sonajeel prospect, nw iran", ***Journal of the Indian Society of Remote Sensing***, Vol. 46, No., (2018), 1581-1593. https://doi.org/10.1007/s12524-018-0811-1
13. Mujabar, P.S. and Dajkumar, S., "Mapping of bauxite mineral deposits in the northern region of saudi arabia by using advanced spaceborne thermal emission and reflection radiometer satellite data", ***Geo-spatial Information Science***, Vol. 22, No. 1, (2019), 35-44. https://doi.org/10.1080/10095020.2018.1530857
14. Sheikhrahimi, A., Pour, A.B., Pradhan, B. and Zoheir, B., "Mapping hydrothermal alteration zones and lineaments associated with orogenic gold mineralization using aster data: A case study from the sanandaj-sirjan zone, iran", ***Advances in Space Research***, Vol. 63, No. 10, (2019), 3315-3332. http://dx.doi.org/10.1016/j.asr.2019.01.035
15. Son, Y.-S., Kim, K.-E., Yoon, W.-J. and Cho, S.-J., "Regional mineral mapping of island arc terranes in southeastern mongolia using multi-spectral remote sensing data", ***Ore Geology Reviews***, Vol. 113, (2019), 103106. https://doi.org/10.1016/j.oregeorev.2019.103106
16. Chattoraj, S.L., Prasad, G., Sharma, R.U., van der Meer, F.D., Guha, A. and Pour, A.B., "Integration of remote sensing, gravity and geochemical data for exploration of cu-mineralization in alwar basin, rajasthan, india", ***International Journal of Applied Earth Observation and Geoinformation***, Vol. 91, (2020), 102162. https://doi.org/10.1016/j.jag.2020.102162
17. Rowan, L.C. and Mars, J.C., "Lithologic mapping in the mountain pass, california area using advanced spaceborne thermal emission and reflection radiometer (ASTER) data", ***Remote Sensing of Environment***, Vol. 84, No. 3, (2003), 350-366. https://doi.org/10.1016/S0034-4257(02)00127-X
18. Tangestani, M. and Moore, F., "Comparison of three principal component analysis techniques to porphyry copper alteration mapping: A case study, meiduk area, kerman, iran", ***Canadian Journal of Remote Sensing***, Vol. 27, No. 2, (2001), 176-182. https://doi.org/10.1080/07038992.2001.10854931
19. Kruse, F.A., Boardman, J.W. and Huntington, J.F., "Comparison of airborne hyperspectral data and eo-1 hyperion for mineral mapping", ***IEEE transactions on Geoscience and Remote Sensing***, Vol. 41, No. 6, (2003), 1388-1400. https://doi.org/10.1109/TGRS.2003.812908
20. Gersman, R., Ben-Dor, E., Beyth, M., Avigad, D., Abraha, M. and Kibreab, A., "Mapping of hydrothermally altered rocks by the eo-1 hyperion sensor, northern danakil depression, eritrea", ***International Journal of Remote Sensing***, Vol. 29, No. 13, (2008), 3911-3936. https://doi.org/10.1080/01431160701874587
21. Bedini, E., Van Der Meer, F. and Van Ruitenbeek, F., "Use of hymap imaging spectrometer data to map mineralogy in the rodalquilar caldera, southeast spain", ***International Journal of Remote Sensing***, Vol. 30, No. 2, (2009), 327-348. https://doi.org/10.1080/01431160802282854
22. Mars, J.C., "Mineral and lithologic mapping capability of worldview 3 data at mountain pass, california, using true-and false-color composite images, band ratios, and logical operator algorithms", ***Economic Geology***, Vol. 113, No. 7, (2018), 1587-1601. https://doi.org/10.5382/econgeo.2018.4604
23. Bolouki, S.M., Ramazi, H.R., Maghsoudi, A., Beiranvand Pour, A. and Sohrabi, G., "A remote sensing-based application of bayesian networks for epithermal gold potential mapping in ahar-arasbaran area, nw iran", ***Remote Sensing***, Vol. 12, No. 1, (2019), 105. https://doi.org/10.5382/econgeo.2018.4604
24. Xiao-chang, M., Wen-can, L., Jian-guo, D. and Wei, X., "Comparison between etm+ and aster data for extraction of alteration information: A case study of fenghuangshan orefield, tongling, anhui province", ***Geoscience***, Vol. 19, No. 2, (2005), 309.
25. WU, Z., GUO, F., LIU, L., Xie, C. and Jiang, Y., "Application of remote sensing alteration anomaly extraction with the method of composite algorithm based on tm/etm images", ***Geology and Exploration***, Vol. 49, No. 3, (2013), 511-522.
26. Pilong, S., Bihong, F., Yuanxu, M. and Qiang, G., "Remote sensing detection for surface anomalies related to hydracarbon in bashibulake uranium ore, sourthern tianshan", in 2016 IEEE International Geoscience and Remote Sensing Symposium (IGARSS), IEEE., (2016), 6374-6377.
27. Adiri, Z., El Harti, A., Jellouli, A., Lhissou, R., Maacha, L., Azmi, M., Zouhair, M. and Bachaoui, E.M., "Comparison of landsat-8, aster and sentinel 1 satellite remote sensing data in automatic lineaments extraction: A case study of sidi flah-bouskour inlier, moroccan anti atlas", ***Advances in Space Research***, Vol. 60, No. 11, (2017), 2355-2367. http://dx.doi.org/10.1016/j.asr.2017.09.006
28. Rajendran, S. and Nasir, S., "Characterization of aster spectral bands for mapping of alteration zones of volcanogenic massive sulphide deposits", ***Ore Geology Reviews***, Vol. 88, No., (2017), 317-335. https://doi.org/10.1016/j.oregeorev.2017.04.016
29. Govil, H., Gill, N., Rajendran, S., Santosh, M. and Kumar, S., "Identification of new base metal mineralization in kumaon himalaya, india, using hyperspectral remote sensing and hydrothermal alteration", ***Ore Geology Reviews***, Vol. 92, (2018), 271-283. https://doi.org/10.1016/j.oregeorev.2017.11.023
30. Abubakar, A.J.a., Hashim, M. and Pour, A.B., "Remote sensing satellite imagery for prospecting geothermal systems in an aseismic geologic setting: Yankari park, nigeria", ***International Journal of Applied Earth Observation and Geoinformation***, Vol. 80, (2019), 157-172. https://doi.org/10.1016/j.jag.2019.04.005
31. Guha, A., Yamaguchi, Y., Chatterjee, S., Rani, K. and Vinod Kumar, K., "Emittance spectroscopy and broadband thermal remote sensing applied to phosphorite and its utility in geoexploration: A study in the parts of rajasthan, india", ***Remote Sensing***, Vol. 11, No. 9, (2019), 1003. https://doi.org/10.3390/rs11091003
32. Pour, A.B., Hashim, M., Hong, J.K. and Park, Y., "Lithological and alteration mineral mapping in poorly exposed lithologies using landsat-8 and aster satellite data: North-eastern graham land, antarctic peninsula", ***Ore Geology Reviews***, Vol. 108, (2019), 112-133. http://dx.doi.org/10.1016/j.oregeorev.2017.07.018
33. Beiranvand Pour, A., Park, Y., Crispini, L., Läufer, A., Kuk Hong, J., Park, T.-Y.S., Zoheir, B., Pradhan, B., Muslim, A.M. and Hossain, M.S., "Mapping listvenite occurrences in the damage zones of northern victoria land, antarctica using aster satellite remote sensing data", ***Remote Sensing***, Vol. 11, No. 12, (2019), 1408. https://doi.org/10.3390/rs11121408
34. Zoheir, B., El-Wahed, M.A., Pour, A.B. and Abdelnasser, A., "Orogenic gold in transpression and transtension zones: Field and remote sensing studies of the barramiya–mueilha sector, egypt", ***Remote Sensing***, Vol. 11, No. 18, (2019), 2122. doi. https://doi.org/10.3390/rs11182122
35. Zoheir, B., Emam, A., Abdel-Wahed, M. and Soliman, N., "Multispectral and radar data for the setting of gold mineralization in the south eastern desert, egypt", ***Remote Sensing***, Vol. 11, No. 12, (2019), 1450. doi. https://doi.org/10.3390/rs11121450
36. Crosta, A., De Souza Filho, C., Azevedo, F. and Brodie, C., "Targeting key alteration minerals in epithermal deposits in patagonia, argentina, using aster imagery and principal component analysis", ***International Journal of Remote Sensing***, Vol. 24, No. 21, (2003), 4233-4240. doi. https://doi.org/10.1080/0143116031000152291
37. Dai, J.-J., Wang, R.-J., Wang, R.-S., Qu, X.-M., Zhao, Y.-Y. and Xin, H.-B., "Porphyry copper deposit prognosis in the middle part of the bangong co-nujiang river metallogenic belt in tibet based

on alteration information extraction", ***Diqiu Xuebao(Acta Geoscientica Sinica)***, Vol. 33, No. 5, (2012), 755-762. doi. https://doi.org/10.1111/rge.12154

38. Yang, R., Li, Z. and Cheng, X., "Information extraction of typical alteration mineral assemblage in porphyry copper using aster satellite data, arequipa province of south peru", ***Journal of Geo-Information Science***, Vol. 14, No. 3, (2012), 411-418. https://doi.org/10.3724/SP.J.1047.2012.00411
39. Zoheir, B. and Emam, A., "Field and aster imagery data for the setting of gold mineralization in western allaqi–heiani belt, egypt: A case study from the haimur deposit", ***Journal of African Earth Sciences***, Vol. 99, (2014), 150-164. https://doi.org/10.1016/j.jafrearsci.2013.06.006
40. Kumar, C., Shetty, A., Raval, S., Sharma, R. and Ray, P.C., "Lithological discrimination and mapping using aster swir data in the udaipur area of rajasthan, india", ***Procedia Earth and Planetary Science***, Vol. 11, (2015), 180-188. https://doi.org/10.1016/j.proeps.2015.06.022
41. Eldosouky, A.M., Abdelkareem, M. and Elkhateeb, S.O., "Integration of remote sensing and aeromagnetic data for mapping structural features and hydrothermal alteration zones in wadi allaqi area, south eastern desert of egypt", ***Journal of African Earth Sciences***, Vol. 130, (2017), 28-37. https:// doi:10.1016/j.jafrearsci.2017.03.006
42. Fereydooni, H. and Mojeddifar, S., "A directed matched filtering algorithm (dmf) for discriminating hydrothermal alteration zones using the aster remote sensing data", ***International Journal of Applied Earth Observation and Geoinformation***, Vol. 61, (2017), 1-13. https://doi.org/10.1016/j.jag.2017.04.010
43. Beiranvand Pour, A., Park, T.-Y.S., Park, Y., Hong, J.K., Zoheir, B., Pradhan, B., Ayoobi, I. and Hashim, M., "Application of multi-sensor satellite data for exploration of zn–pb sulfide mineralization in the franklinian basin, north greenland", ***Remote Sensing***, Vol. 10, No. 8, (2018), 1186. doi: 10.3390/rs10081186.
44. Noori, L., Pour, A.B., Askari, G., Taghipour, N., Pradhan, B., Lee, C.-W. and Honarmand, M., "Comparison of different algorithms to map hydrothermal alteration zones using aster remote sensing data for polymetallic vein-type ore exploration: Toroud–chahshirin magmatic belt (TCMB), north iran", ***Remote Sensing***, Vol. 11, No. 5, (2019), 495. doi: 10.3390/rs11050495.
45. Chen, Q., Zhao, Z., Jiang, Q., Zhou, J.-X., Tian, Y., Zeng, S. and Wang, J., "Detecting subtle alteration information from aster data using a multifractal-based method: A case study from wuliang mountain, sw china", ***Ore Geology Reviews***, Vol. 115, (2019), 103182. doi: 10.1016/j.oregeorev.2019.103182.
46. Stöcklin, J., Eftekharnezhad, J. and Hushmandzadeh, A., *Central lut reconnaissance east iran, geological survey of iran*. 1972, Report.
47. Camp, V. and Griffis, R., "Character, genesis and tectonic setting of igneous rocks in the sistan suture zone, eastern iran", ***Lithos***, Vol. 15, No. 3, (1982), 221-239. doi: 10.1016/0024-4937(82)90014-7.
48. Tirrul, R., Bell, I., Griffis, R. and Camp, V., "The sistan suture zone of eastern iran", ***Geological Society of America Bulletin***, Vol. 94, No. 1, (1983), 134-150. http://dx.doi.org/10.1130/0016-606(1983)94<134:TSSZOE>2.0.CO;2
49. Beygi, S., Talovina, I.V., Tadayon, M. and Pour, A.B., "Alteration and structural features mapping in kacho-mesqal zone, central iran using aster remote sensing data for porphyry copper exploration", ***International Journal of Image and Data Fusion***, Vol. 12, No. 2, (2021), 155-175. doi: 10.1080/19479832.2020.1838628.
50. Hunter, E. and Power, C., "An assessment of two classification methods for mapping thames estuary intertidal habitats using casi data", ***International Journal of Remote Sensing***, Vol. 23, No. 15, (2002), 2989-3008. https://doi.org/10.1080/01431160110075596
51. De Carvalho, O.A. and Meneses, P.R., "Spectral correlation mapper (scm): An improvement on the spectral angle mapper (sam)", in Summaries of the 9th JPL Airborne Earth Science Workshop, JPL Publication 00-18, JPL publication Pasadena, CA, USA. Vol. 9, No. Issue, (2000), 2.
52. Gabr, S., Ghulam, A. and Kusky, T., "Detecting areas of high-potential gold mineralization using aster data", ***Ore Geology Reviews***, Vol. 38, No. 1-2, (2010), 59-69. doi. https://doi.org/10.1016/j.oregeorev.2010.05.007

Persian Abstract

چکیده

در این تحقیق از تصاویر ماهواره‌ای ASTER و الگوریتم ترکیبی نسبت‌های باند با روش عملگرهای منطقی با تعیین حد آستانه بر اساس مطالعات میدانی، آزمایشگاهی و تجربی به منظور برجسته‌سازی دگرسانی های هیدروترمال استفاده شده است. تکنیک‌های تبدیل تصویر مانند نسبت باند تخصصی و تحلیل مؤلفه‌های اصلی برای نقشه‌برداری واحدهای سنگ‌شناسی و کانی‌های دگرسانی استفاده می‌شوند. تکنیک طبقه‌بندی نظارت‌شده، نقشه‌برداری زاویه طیفی (SAM) برای تشخیص تفاوت‌های ظریف بین کانی‌های شاخص دگرسانی مرتبط با محل‌های واقعی مس در منطقه اعمال می‌شود. نتایج نشان می‌دهد که ادغام تکنیک‌های تبدیل تصویر و طبقه‌بندی نظارت شده داده‌های ASTER با مطالعات میدانی و اکتشافات ژئوشیمیایی در پی جویی کانی‌سازی جدید مس بسیار موثر است. کانی‌سازی مس در محدوده همراه با رگه‌های سیلیسی مشاهده می‌شود. روند عمومی رگه‌های سیلیسی حاوی کانی‌زایی مس شمال–جنوبی تا شمال شرقی–جنوب غربی می‌باشد. شواهد دورسنجی وجود دگرسانی پروپیلیتی و آرژیلیک را تایید می‌کند که می‌تواند برای پی‌جویی کانسارهای نوع مس–طلا مفید باشد. کائولینیت و پیروفیلیت در شناسایی زون‌های دگرسانی آرژیلیک نقش دارند و کانی‌های مسکوئیت، اپیدوت و کلریت در شناسایی زون‌های پیروپیلیتیک و فیلیک و در بحث اکتشاف مواد معدنی اهمیت فراوانی دارند. بر اساس پردازش های دورسنجی، با توجه به تشخیص دگرسانی‌های مختلف (فیلیک، پیروفیلیت و آرژیلیک) وسیع در این ناحیه، تشخیص کانی زایی احتمالی مس در بخش میانی منطقه مورد مطالعه حاصل شد. رویکرد مورد استفاده در این تحقیق ابزاری سریع و مقرون به صرفه برای شروع برنامه‌های اکتشافی جامع زمین‌شناسی و ژئوشیمیایی در منطقه مورد مطالعه و در مناطق مشابه فراهم می‌کند.